AIAA JOURNAL
Vol. 30, No. 7, July 1992

Eigenfunction Analysis of Turbulent Mixing Phenomena

M. Winter* and T. J. Barber†
United Technologies Research Center, East Hartford, Connecticut 06108
and
R. M. Everson‡ and L. Sirovich‡
Brown University, Providence, Rhode Island 02912

An analysis of the inviscid mixing of a turbulent jet in crossflow is considered. An experimental data base is analyzed by means of a technique based on the empirical eigenfunctions. It is shown, for example, that mixing that increases with downstream distance is characterized by patterns of increasing complexity. A firm quantitative basis is presented that supports this visual perception of complexity.

Nomenclature

A = area
a_j = jth eigenfunction coefficient
c = scalar concentration
D_1 = complexity
D_2 = weighted complexity
E = energy
K = correlation function
k = wave number
N = ensemble size
p_n = probability
S = length of nodal line
t = time
x = position
z = axial position
ϵ = energy
λ_n = eigenvalue of order n
σ = spectral entropy
ϕ_n = eigenfunction of order n

Introduction

MIXING processes play a vital role in the operation of combustion systems for airbreathing propulsion systems. This paper is primarily concerned with the nature and description of these mixing processes, including providing the development of a framework, some tools, and even a language by which to discuss mixing in quantitative terms. A longer range goal of this research is to develop methods and criteria for the management of the mixing process. Although the principal focus is applied to a specific gas turbine combustor problem, the methodology developed is equally applicable to virtually every aspect of technology and engineering where mixing processes are important.

As an example of a mixing-dominated problem, one can consider the gas turbine combustor. The design and performance of a gas turbine combustor requires good mixing characteristics to achieve high burning rates, low soot/NO_x formation, and exhaust temperature uniformity. Typically, however, complete mixing can only be accomplished at the expense of combustor length and pressure loss. A gas turbine combustor flow path is characterized by three distinct zones[1]: a primary zone where combustion occurs, an intermediate zone where mixing-driven species recombination (to lower gas temperatures) occurs, and a dilution zone where coolant air is injected and mixed with the combustion gases to achieve a desired turbine inlet temperature. Current designs for the dilution zone resort to a series of round jets, injecting cold air at right angles to the primary gas flow to achieve the highest degree of mixing. The rate of mixing, however, is strongly influenced by the hole shape, momentum ratio of the jet/primary flow, turbulence level, axial distance, etc. To date, mixing optimization has been largely an empirical process, and any assessment of induced mixing has been indirectly inferred. The present study will focus on a model problem of the dilution zone, viz., a subsonic jet in a crossflow. As a result of the relative pressure difference between the bypass and the hot combustor flow, mass is entrained into the combustor flowfield. The entrained flow effectively acts as a jet in crossflow. Such problems have been previously studied experimentally by Vranos and Liscinsky.[2] In their experiment, advanced data acquisition techniques using optically based diagnostics[3] furnish us with a wealth of detailed and highly resolved data.

Although the data that will be analyzed next are from a physical experiment, the methodology presented is applicable generally and could just as easily have been applied to a computationally generated data base. An additional feature of the investigation relates to the treatment of large data bases in general. Our methods give a format for analyzing these, and perhaps of equal importance we present a method that permits substantial data compression. As will be seen, all of this is accomplished by generating an intrinsically defined basis set of describing functions, which in a well-defined sense are optimal.

Preliminary Results

Although it is not necessary to restrict attention to two dimensions, all of our deliberations will refer to concentration fields in two-dimensional slices, z = const, of a flow. We will denote the fluctuation in a concentration at a time t by $c(\boldsymbol{x},t)$ where $\boldsymbol{x} = (x,y)$ is a position in the plane. If we denote a time average by

$$\langle c \rangle = \frac{1}{T}\int_{-T/2}^{T/2} c(\boldsymbol{x},t)\, dt \tag{1}$$

then the fluctuation is defined such that

$$\int_A \langle c(\boldsymbol{x}) \rangle\, d\boldsymbol{x} = 0 \tag{2}$$

Presented at the AIAA 29th Aerospace Sciences Meeting, Reno, NV, Jan. 7-10, 1991; received May 28, 1991; revision received Nov. 4, 1991; accepted for publication Nov. 18, 1991.

*Research Scientist. Member AIAA.
†Manager, Physical and Mathematical Modeling. Member AIAA.
‡Professor, Center for Fluid Mechanics and Division of Applied Mathematics.

where A denotes the area of the slice. Instantaneous averaging,

$$c_A(t) = \frac{1}{A}\int c(x,t)\,dx \tag{3}$$

is not necessarily a constant. Perhaps the coarsest and most widespread measure of a passive scalar concentration field is its rms value:

$$\bar{c}(x) = \langle c^2(x)\rangle^{1/2} \tag{4}$$

The smaller the average value of $\bar{c}$,

$$c_{rms} = \frac{1}{A}\int_A \bar{c}(x)\,dx \tag{5}$$

the better the mixing. Although Eq. (3) furnishes us with information that locates and measures the fluctuations, it does not address the issue of what are the scales of the fluctuations. This is of great importance since the *texture* of the concentration field determines how soon molecular diffusion plays its final role. When viewing fine grain vs coarse grain fluctuations of equal magnitude, it is clear that the former is more rapidly mixed than the latter.

This simple observation suggests that finer measures of mixedness should be employed. For example, if it makes sense to speak of the Fourier transform of $c(x)$, $\tilde{c}(k)$, then we can use the spectral entropy

$$\sigma = -\int \epsilon(k)\,\ell n\,\epsilon(k)\,dk, \qquad \epsilon = |\tilde{c}|^2/c_{rms}^2 \tag{6}$$

where $\epsilon(k)$ is the energy at wave number k. Two other measures that will be discussed later are

$$D_1 = \frac{1}{A}\int \frac{|\nabla c|\,dx}{c_{rms}} \tag{7}$$

$$D_2 = \frac{1}{A}\int \frac{|\nabla c|^2\,dx}{c_{rms}^2} \tag{8}$$

The first of these, Eq. (6), addresses the diversity of scales, while Eqs. (7) and (8) bring out the importance of small scales in mixing. It should be noted that both Eqs. (7) and (8) are dimensional and should be normalized with respect to the Kolmogorov scale. More specifically, we are addressing that part of the mixing process that is inviscid (large scale) and that precedes molecular diffusion (small scale).

A shortcoming of the previous discussion is the absence of *physics*, more specifically the isolation of basic patterns by which the mixing process takes place. If the mixing process can itself be decomposed into fundamental patterns or modes of mixing, then we can hope to proceed to the goal of managing the mixing process by manipulating these fundamental modes.

Karhunen-Loeve (*K-L*) Procedure

The *K-L* procedure was proposed by Lorenz[4] and by Lumley[5] for the analysis of turbulence data, in the former instance to treat meteorological data, and in the latter case to isolate coherent structures. In each instance time series or their equivalent were considered. In recent years it has been shown that fully three-dimensional phenomena can be treated by this method.[6,7] This has been accomplished by the method of *snapshots* that we now briefly develop within the framework of the jet in crossflow, which we analyze in detail in the Results section.

We consider the fluctuation field in a plane orthogonal to the jet and denote it, as earlier, by $c(x,t)$. We assume that the mean value has been subtracted so that Eq. (2) is satisfied. The concentration fluctuation is captured *instantaneously* at a uniformly spaced sequence of instants and the resulting ensemble of such states is denoted by

$$\{c^{(n)}\} = \{c^{(n)}(x)\} = \{c(x,t_n)\} \tag{9}$$

where as indicated the superscript denotes the instant of time. Typical concentration profiles are shown in Fig. 1.

To develop the *K-L* procedure we pose the following question: Is there some *concentration profile* that is most typical? Stated analytically, for what ϕ is

$$\langle(\phi,c)^2\rangle = \frac{1}{N}\sum_{n=1}^{N}\left[\int \phi(x,y)c^{(n)}(x,y)\,dx\,dy\right]^2 \tag{10}$$

a maximum? (Note that the time average is replaced by a discrete average.) For this to make sense there must be some constraint on ϕ; e.g., since we regard ϕ as a *concentration fluctuation*, we require

$$\|\phi\|^2 = (\phi,\phi) = \langle(c,c)\rangle = c_{rms}^2 = E \tag{11}$$

although any such requirement will suffice. (In the following, E will be termed the *energy*.) The result of the variational problem posed by Eqs. (10) and (11) is that ϕ satisfy

$$\int K(x,x')\phi(x')\,dx' = \lambda\phi(x) \tag{12}$$

where

$$K(x,x') = \langle c(x)c(x')\rangle = \frac{1}{N}\sum_{j=1}^{N} c^{(j)}(x)c^{(j)}(x') \tag{13}$$

is the autocorrelation of the ensemble of concentrations. The eigenfunction equation, Eq. (12), generates a complete set of functions, each of which satisfies the extremal condition of Eqs. (10) and (11), along with the side condition that it be orthogonal to all previously generated eigenfunctions. Without loss of generality we can take the set of eigenfunctions to be an orthonormal set.

A considerable reduction in the complexity of the problem is achieved by recognizing that an eigenfunction that satisfies Eq. (12) with K such that Eq. (11) holds must be an admixture of instantaneous *snapshots*, i.e., we can write

$$\phi(x,y) = \sum_{j=1}^{N} \alpha_j c^{(j)}(x) \tag{14}$$

This reduces the integral equation, which in general may have support in many dimensions, to the relatively simple step of the diagonalization of a matrix of order N. This version of the *K-L* procedure is known as the method of snapshots. As a result of the completeness of the eigenfunctions we can express the time-dependent concentration in terms of the eigenfunctions $\{\phi_n(x)\}$ as follows:

$$c(x,t) = \sum_{n=1}^{\infty} a_n(t)\phi_n(x) \tag{15}$$

where

$$a_n = (\phi_n,c) \tag{16}$$

The set $\{\phi_n\}$ is termed the *empirical eigenfunctions*, and they have the property that the variance

$$\sigma = \langle\|c - \sum_{j=1}^{N} a_n\phi_n\|^2\rangle^{1/2} \tag{17}$$

is minimal (for any N) over the class of all admissible orthonormal basis sets. One additional characterization is that with the empirical eigenfunctions and only with these are the coefficients decorrelated

$$\langle a_n a_m\rangle = 0, \qquad m \neq n \tag{18}$$

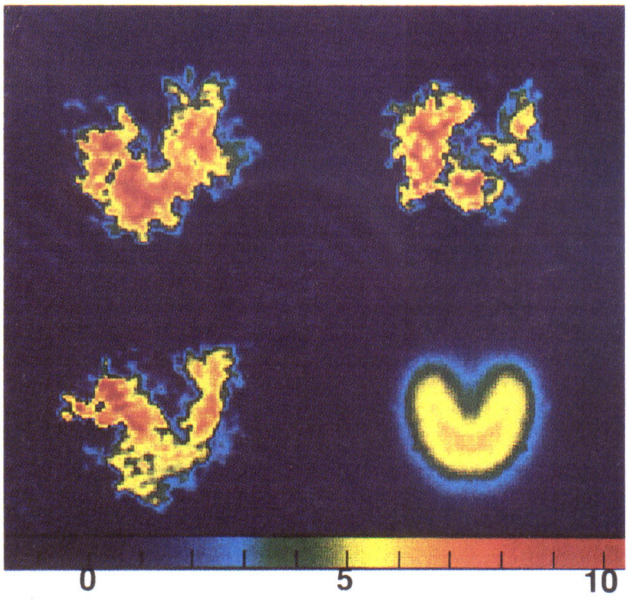

Fig. 1 Three typical cross-sectional snapshots compared with the time-averaged concentration (bottom right) for a subsonic jet in crossflow.

and from this the (information) entropy is minimal amongst all representations.[8] Using this, it follows from the definition of Eq. (13) that

$$\langle a_n^2 \rangle = \lambda_n \tag{19}$$

It may be of some help in understanding the role of the empirical eigenfunctions to consider the following thought experiment. Imagine a data base generated by recording the time series measured at uniformly placed points of a randomly plucked string that is fixed at $x = 0$ and $x = 1$. If, without prior knowledge of how the data base was created, we apply the *K-L* procedure to it, and then the empirical eigenfunctions are found to be the Fourier modes,

$$\{\phi_n(x)\} = \{\sin n\pi x\} \tag{20}$$

which, of course, are the best functions to employ in dealing with the problem of the plucked string. In fact, what has just been described can be used for the determination of eigenfunctions of many linear operators.[9]

As an illustration of the procedure (and one that is mathematically identical to the case that we specifically consider here), we show in Fig. 2 the average face of an ensemble of 125 male faces,[10,11] next to this is a typical face of the ensemble, and next to that the fluctuation of the typical picture (the background gray represents the zero level), termed the caricature (Fig. 2 has been recomputed from the reported data base). Following that we show in Fig. 3 the first six *eigenpictures* as generated by the snapshot method. Note that the eigenpictures are even or odd functions in the midline. This is a result of the fact that the ensemble was doubled in size by adding to the ensemble the mirror image of each member. This artifice, which doubles the ensemble size, brings out a latent symmetry that would otherwise be brought out only in a much larger ensemble. It also applies in our study of the jet in crossflow, since the physical experiment respects this particular symmetry. With these eigenpictures we can represent a typical face in terms of 50 eigenpictures, with an average variance (mean square error) of less than 3%. This is instead of the $\mathcal{O}(10^4)$ pixel gray levels that are required in specifying a typical face as in Fig. 2.

As another illustration and one that is more closely related to the present investigation, we show in Fig. 4 an instantaneous shot of the longitudinal cross section of a turbulent jet.[12] When the previous analysis is applied to this case, we get eigenfunctions of the sort shown in Fig. 5 (Figs. 4 and 5 have been recomputed from the reported data base). The individual eigenfunctions clearly bring out features of the flow.

Data Compression

Since the empirical eigenfunctions are optimal with regard to the representation of phenomena, they are also highly efficient in the *packing of data*. We can imagine a data base generated through experiment or computation. In the context of a turbulent flow, this would mean having data dumps or snapshots of the flowfield at discrete times. For example, we would have snapshots of the flow

$$c^{(n)}(x) = c(x, t_n) \tag{21}$$

The collection of these files $c^{(n)}(x)$ then constitutes the data base. Instead of storing this collection, we can store the set of eigenfunctions $\phi_n(x)$ that was generated by the step-by-step procedure. Then, to within a criterion error tolerance, each snapshot can be stored by approximating it by a finite sum

$$c(x) \approx \sum_{n=1}^{M} a_n \phi_n(x) \tag{22}$$

This procedure entails saving only M eigenfunctions once and an additional M scalars $a_1, a_2, \ldots, a_M$ for each snapshot. Compressions of 50–100 have been achieved[10,11] in this way at the expense of relatively small percentage errors. Illustrations of the compression capability, in terms of relatively few eigenfunctions, have been presented in Refs. 10–12.

Description of Experiment/Data Base

A round jet injected at right angles to a subsonic primary stream induces the characteristic flow structure seen in Fig. 6. Initially, the jet begins with an inviscid or potential core, persisting until viscous mixing effects predominate. The deflection of the jet by the primary stream induces a pair of counter-rotating vortices that result in the familiar kidney-shaped jet cross section on average. An inviscid secondary flow mechanism[13] is responsible for their generation. As indicated in the figure, a horseshoe vortex is also generated by the interaction of the jet with the upstream primary flow boundary layer.

In the initial experiments by Vranos and Liscinsky,[2] the geometry and flow conditions at the boundaries were modeled to facilitate the interpretation of the data and to allow comparison of the results with those of other investigators, i.e., a single jet in cross flow. The apparatus is shown schematically in Fig. 7. The working section consisted of three parallel contiguous ducts of rectangular cross section, simulating a sector of an annular gas turbine combustor. The inner duct

Fig. 2 Average face (over 125 male faces), typical snapshot, and its caricature.

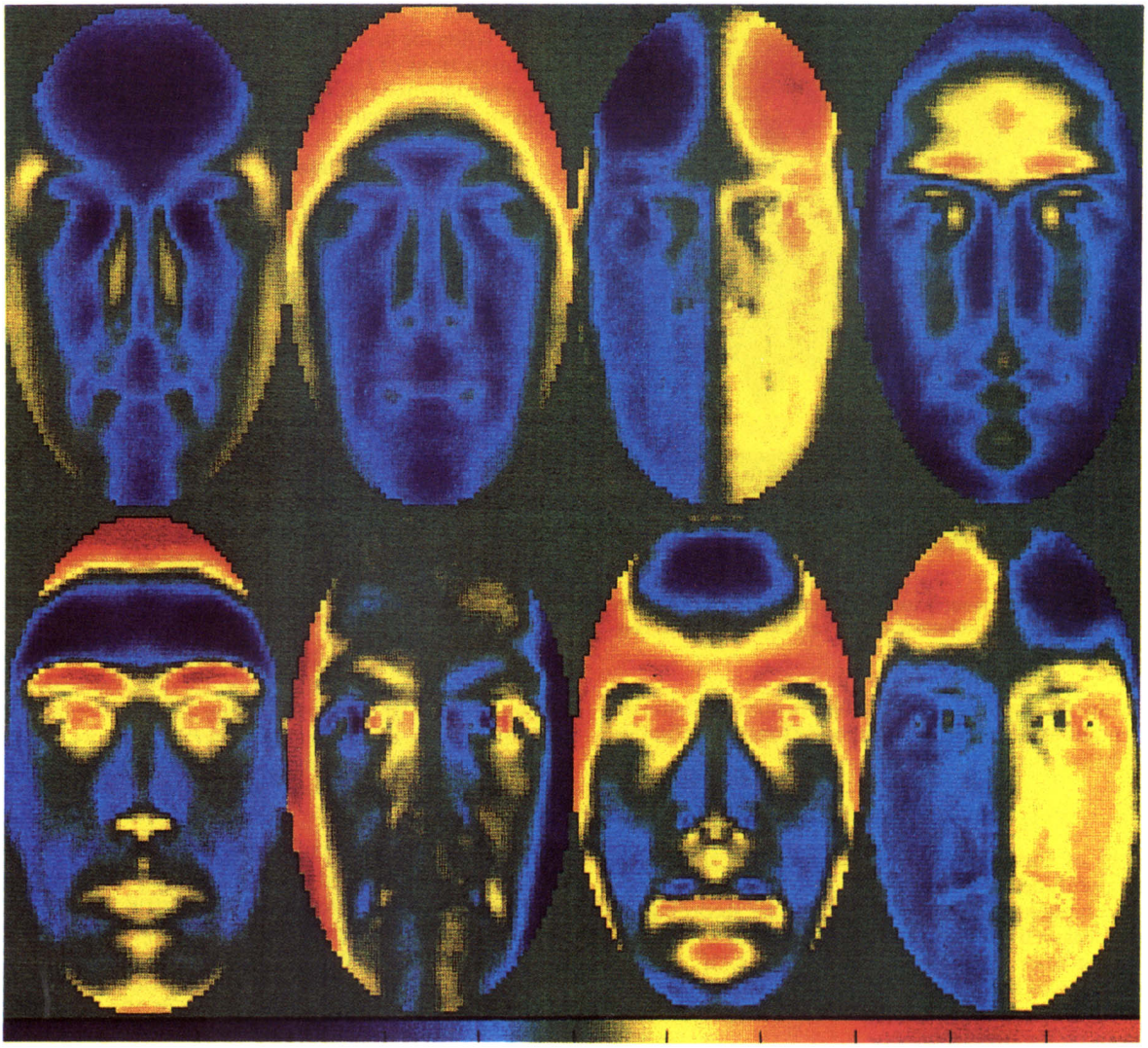

Fig. 3 Six eigenfunctions of 125 male faces.

Fig. 4 First 6 snapshots of an ensemble of 300 snapshots for a turbulent jet (flow is from bottom to top).

was of width 30.5 cm and height 10 cm. Optical access was available from the side through a 30.5 cm × 10 cm × 0.16 cm pyrex window. Air forming the jet was fed through a single orifice in the upper wall of the test section. The hole was beveled inward and brought to a sharp edge at the discharge plane. Gas flows were metered using critical flow orifices, and jet velocities were measured with hot-wire anemometry.

The character of the flow depends on the momentum, $\rho_j V_j^2$, carried by the injected fluid gas to that of the cross flow gas, $\rho_c V_c^2$. This momentum ratio $[M = (\rho_j V_j^2)/(\rho_c V_c^2)]$ was varied by changing the velocity of the injected fluid at constant cross-flow velocity. The experiments were conducted over a Reynolds number range of 50–80,000 based on jet diameter and cross-flow conditions. The working fluid was air at room temperature, and jet velocities were sufficiently low to eliminate compressibility effects.

Planar digital imaging of the light scattered from small aerosol particles was used to ascertain jet concentrations. This technique, known as Lorenz-Mie scattering, is based on the principle that, for a gas seeded uniformly with aerosol particles, the intensity of elastically scattered light from the aerosols is proportional to the concentration of the seeded gas. If the seeded gas mixes with a second unseeded gas, the number of scattering particles is less in a given volume and therefore proportionally less radiation is scattered. Planar digital imaging has been demonstrated as an effective, quantitative diagnostic technique in small laboratory jets by Long et al.[3] Planar nephelometry measurements were made by marking the flowfield with small aerosol particles introduced into the nozzle gas upstream of mixing baffles. A transverse section (z = const) of the flowfield was briefly illuminated by reflecting a beam of unfocused argon-ion laser light with a rotating mirror. The elastically scattered light was imaged onto a low light level vidicon camera and digitized. The fluid motion was frozen by exposing the detector for only 10 μs coincident with a single sweep of the laser beam through the flowfield. The light sheet was approximately 500 μm thick and passed through a transverse slice of the jet at several stations downstream. The

rotation rate of the mirror was sufficiently fast so that all measurements within the frame are considered simultaneous. Each image (data frame) consists of approximately 10,000 data points arranged in a 100×100 pixel format. The raw images were corrected for background response due to detector noise, scattered light, and laser sheet nonuniformity.

The data base we analyze here is composed of three sets of images collected at $z = 4$, 6, and 8 jet diameters downstream from the jet orifice at a momentum ratio M of 15.2 together with additional sets collected at the 8-diam station, one with a higher momentum ($M = 17.5$), and the other with a lower momentum ratio ($M = 6.9$). Each image set consists of approximately $N = 500$ snapshots.

Figure 1 shows three instantaneous realizations and the average 500 realizations at the 6-diam station. In Fig. 8, we show the symmetrized versions of the average concentration fields at the 4-, 6-, and 8-diam stations. For each of the five data bases described, we have doubled the ensemble size by adding to each ensemble the mirror images, in the vertical midline, of each ensemble member. In doing this we are exploiting the natural symmetry that should be present in the flow that is shown in Fig. 6. This addition to the ensemble produces eigenfunctions that are either odd or even in the vertical midline, a result that would not be realized unless the ensemble size becomes relatively large. Comparison of the average at the 6-diam station with its unsymmetrized version shown in the fourth quadrant of Fig. 1 illustrates the strong tendency toward mirror symmetry.

Although the data represent the large-scale flow structure well in the concentration profiles, a considerable degree of noise and drift were present in the images. To standardize this large data base for comparison between different experimental conditions and data acquired over long periods of time, the data were normalized in the following manner. A reference value for each snapshot was determined from a 10×10 pixel area containing no seeded fluid in the corner of each snapshot. A systematic drift in the measured concentration was eliminated based on these values, and the data were then rescaled so that the mean concentration flux through each picture was constant. In addition, filtering in Fourier space was used to remove some background noise. Although this renormalization changes the concentration values and hence the dynamic range, the macroscopic flow structure remains preserved. Present plans call for further experimentation in a more controlled manner.

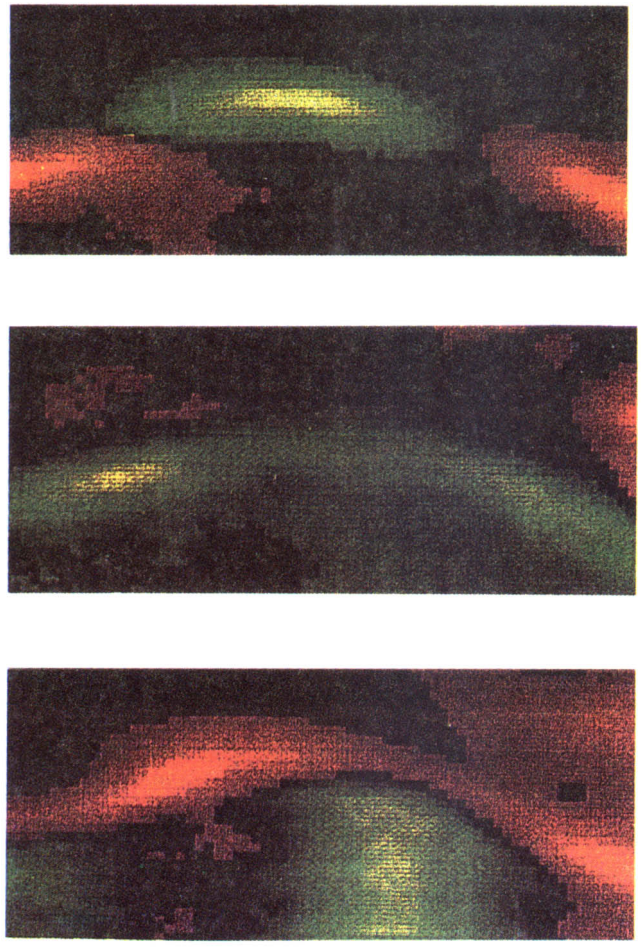

Fig. 5 First three eigenfunctions of the turbulent jet shown in Fig. 4.

Results and Discussion

The *K-L* procedure described earlier is now applied to the various cross-flow jet data that was described in the previous section. In all instances we deal only with the fluctuation from the average concentration. Typical snapshots of the set cross section have been shown in Fig. 1. In presenting the eigenfunctions we will typically arrange them in descending order of the magnitude of the eigenvalues, Eq. (19). Each eigenvalue is a measure of the degree to which the corresponding eigenfunction has been excited. If we divide the eigenvalues by the energy, Eq. (11),

$$p_n = \lambda_n / E \tag{23}$$

then p_n can be interpreted as being a probability. It tells us the probable degree to which the jet cross section is in the state described by $\phi_n(\boldsymbol{x})$. Figure 9 contains the first 12 eigenfunctions for the low momentum ensemble. We have chosen this case to illustrate the nature of the eigenfunctions both because of the *lower degree of complexity* that results from its low momentum ratio and the relatively high signal-to-noise ratio. As a result of the former, the seed concentration is still poorly mixed, and the eigenfunctions then are naturally arranged in order of increasing *mixedness* by their corresponding eigenvalues. The first eigenfunction shown reflects the fact that although $\langle c \rangle = 0$, at any instant the concentration need not have a zero spatial average since temporal pulsations are present in general; see Eq. (3). The second most probable eigenfunction allows for bilateral variation. It has two *cells*, the third has three cells, and the fourth has four cells. The complexity and cell number is seen to increase as we proceed

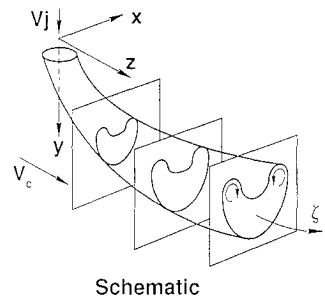

Fig. 6 Schematic diagram of a subsonic jet in crossflow.

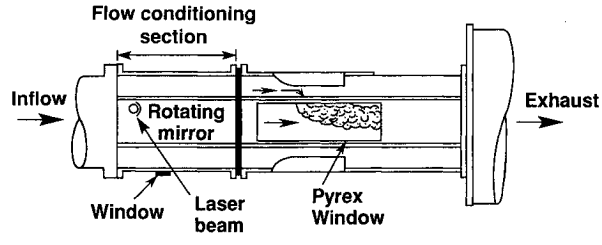

Fig. 7 Schematic diagram of jet in crossflow experimental facility.

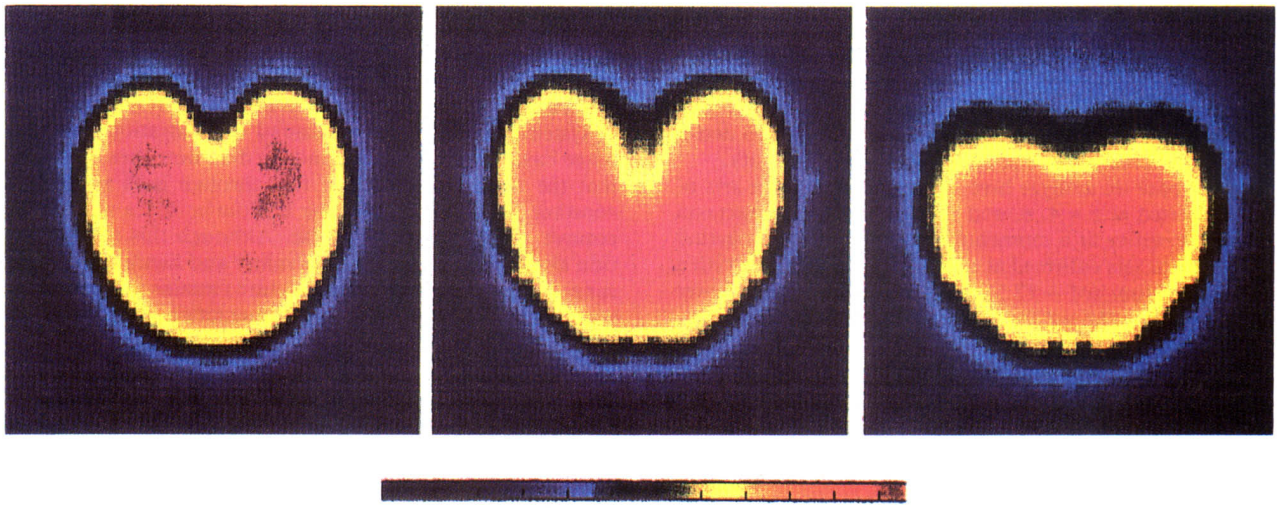

Fig. 8 Symmetrized cross-sectional averages for the 4-, 6-, and 8-diam stations.

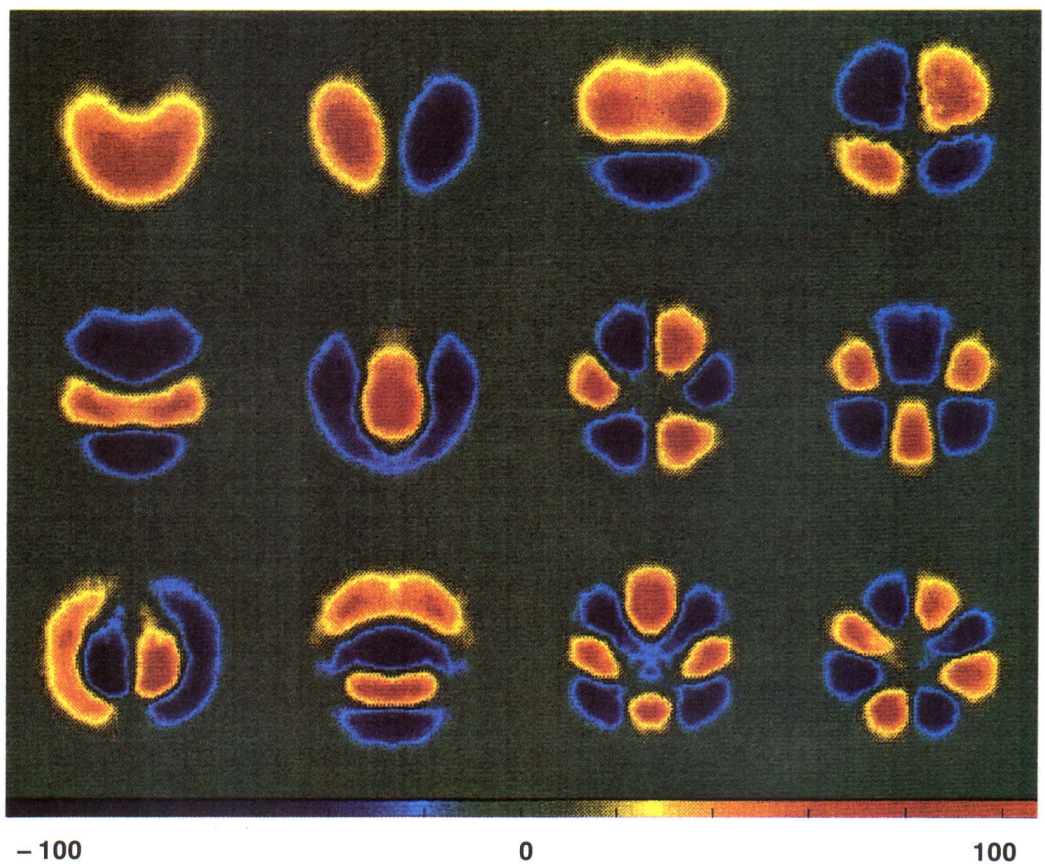

Fig. 9 First 12 empirical eigenfunctions from the low momentum ratio ensemble (scale ± 100).

through the list of eigenfunctions. On the basis of the principal eigenfunctions, as we move down the list of eigenfunctions we see the possibility of increasing breakdown in the length scale by increasing complexity in the patterns. The notion of complexity is visual at this point and will be made more precise later in this section. Figure 10 shows the first five eigenfunctions, derived from data collected at the 4-, 6-, and 8-diam stations, arranged in rows. The first row corresponds to the section closest to the jet, where the mixing is poorest. There is, in fact, a close resemblance between the first row and Fig. 9.

We adopt as a reasonable criterion for well mixedness that more highly complex patterns become more probable. This would require, for example, the retention of more terms in Eq. (22). Such a trend is apparent from the rows of eigenpictures in Fig. 10. On visual grounds it is apparent that mode crossing is taking place and that at 8 diameters downstream the dominant pattern is made up of four cells. As we move down the three rows, we see increasing complexity developing, reflecting progressive mixing as we move downstream.

Our use of the term *complexity* has been based, thus far, on visual appearance. We next make this notion more precise by defining several different measures of complexity. The first of these, termed the S complexity, is based on the total length of the nodal lines of a function. In Fig. 11 we show the nodal lines that correspond to the eigenfunctions of Fig. 9. Simple functions, with few *cells*, have short nodal lines whereas convoluted functions have correspondingly longer nodal lines. In practice, the nodal line depends sensitively on the amount of

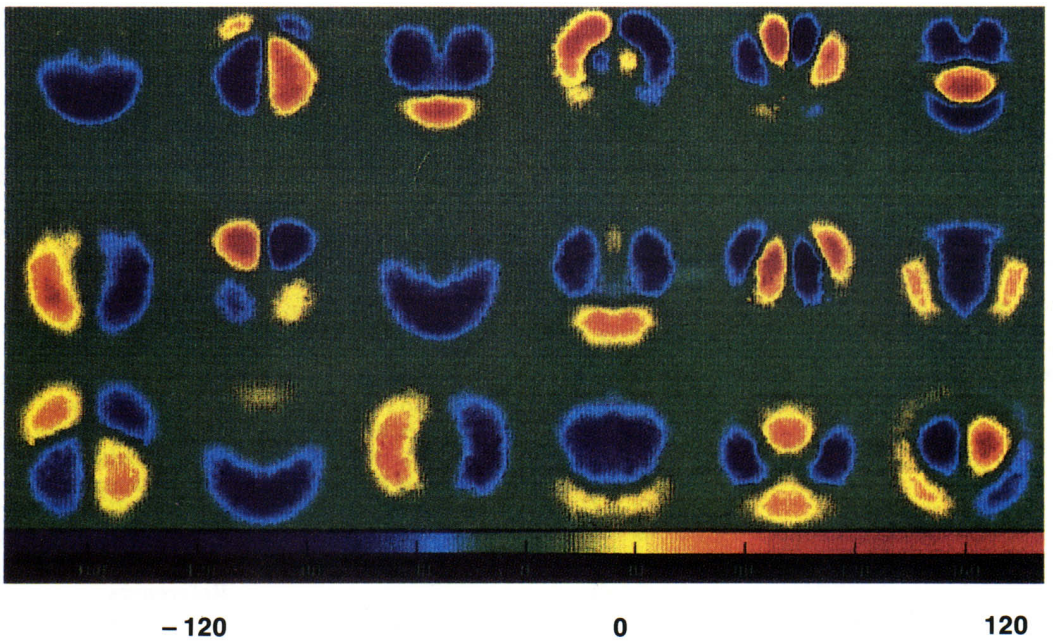

Fig. 10 Comparison of the first five eigenfunctions ordered by the associated eigenvalue with the most energetic at the left (scale ± 120).

experimental noise that contributes extraneous zero crossings and we prefer to use contours at criterion heights $\pm z$:

$$S(\phi) = \frac{1}{2A^{1/2}}\left(\int_{\gamma(z)} dl + \int_{\gamma(-z)} dl\right) \tag{24}$$

where $\gamma(z)$ denotes the level curve of $\phi(x,y)$ at height z. The S complexity is normalized by $A^{1/2}$, the square root of the area of the eigenvalue picture, and is therefore dimensionless. The S complexity fails to account for the characteristics of the eigenpictures that do not intersect the level curves $\gamma(\pm z)$. Two measures that may be regarded as the sum of the lengths of all of the level curves are

$$D_1 = \frac{1}{A^{1/2}}\int |\nabla\phi|\, dA \tag{25}$$

and

$$D_2 = \int (\nabla\phi)^2\, dA \tag{26}$$

Both of these measures, which have been defined to be dimensional, are equivalent to Eqs. (6) and (7).

The second of these is weighted by $\nabla\phi$ to emphasize level lines passing through regions where the function changes rapidly. These measures, too, are susceptible to experimental noise propagated through to the eigenpicture. However, an initial smoothing (by filtering in Fourier space) of the experimental snapshots yields broad agreement between D_1 and D_2.

The spectral entropy, previously given by Eq. (5), is given by

$$\sigma = -\int \epsilon(\boldsymbol{k}) \ln \epsilon(\boldsymbol{k})\, d\boldsymbol{k} \tag{27}$$

where $\epsilon(\boldsymbol{k})$, the energy at wave number $\boldsymbol{k}$, is the square magnitude of the Fourier transform of $\phi(\boldsymbol{x})$. It follows therefore that $\epsilon(\boldsymbol{k})$ is a probability, i.e.,

$$\int \epsilon(\boldsymbol{k})\, d\boldsymbol{k} = 1 \tag{28}$$

The one-dimensional form of Eq. (27) has been used to characterize the complexity of certain patterns occurring in thermal convection.[14] If the eigenpicture is a single Fourier mode, then the spectral entropy is zero, whereas if the energy is distributed uniformly amongst all of the modes, then $\sigma \to 1$. Note that the spectral entropy does not distinguish between high and low wave-number modes and for this reason is less useful than Eqs. (25) or (26) for purposes of assessing mixedness.

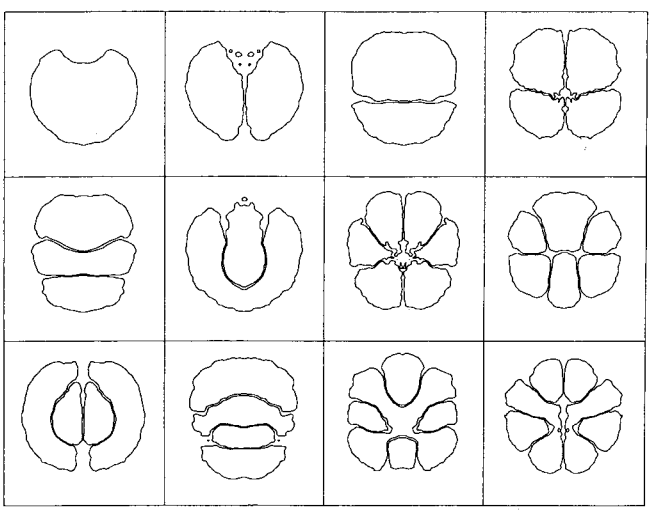

Fig. 11 Nodal lines derived from the low momentum ratio data set used to determine S complexity.

There is broad agreement between the orderings of the eigenpictures according to the D_1, D_2, and σ measures. Figure 12 shows the first few eigenvalues at 4-, 6-, and 8-diam stations, plotted in order of increasing D_2 complexity of the corresponding eigenpicture. At the 4-diam station, the simplest, almost dc, eigenfunction contributes most to the flow. Increasingly complex eigenfunctions carry decreasing energies. At the 6-diam station, there is no longer an almost dc eigenfunction, and the mode carrying the most energy has two cells and odd symmetry about the centerline. Additionally, the second largest eigenvalue corresponds to the sixth least simple eigenpicture. This four-celled mode (also recognizable as the second eigenpicture at the 4-diam station) carries most energy at the 8-diam station. Simpler eigenpictures contribute less to

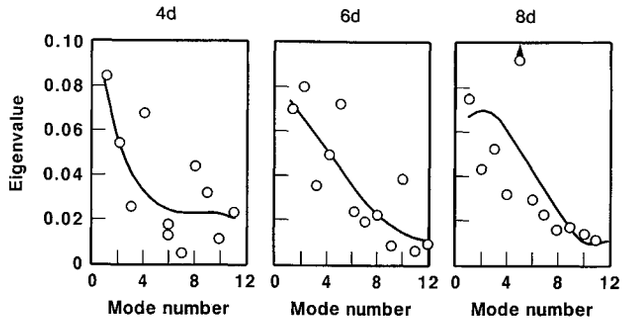

Fig. 12 Eigenvalue number 4-, 6-, and 8-diam stations plotted in order of increasing D_2 complexity of the corresponding eigenvalue.

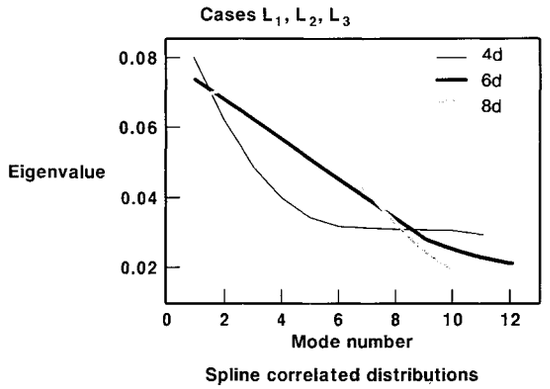

Fig. 13 Coplotted spline smoothed eigenvalue distributions.

the flow's structure, indicating a more complex, better mixed flow.

Conclusions

This paper has focused on the problem of mixing and mixing assessment. More specifically, it makes the following observations:

1) The technique of "empirical eigenfunctions" has been developed and applied to the analysis of a mixing dominated flow. A language coupling mixedness with pattern structure was developed and quantitative measures of mixedness defined.

2) The technique has demonstrated a method for extracting a maximum degree of flow physics from advanced nonintrusive diagnostic data. Individual snapshots of data can now be interrogated for mixing scales and levels.

3) The technique was applied to a jet in crossflow and quantitatively verified one's intuitive expectations of a most mixed state, i.e., the flow is better mixed further downstream, higher jet momentum ratios mean more mixing. In particular, by disregarding the effect of data scatter (by cubic spline fitting data from Fig. 12), one can quickly observe in Fig. 13 the effect of increased downstream distance on mixing in the growth of complexity with distance.

4) An observation is made that the greatest level of mixedness correlates with activating modes with greater complexity. A sensitive *metric* of the mixedness of a flow is afforded by assessing the probability with which complex modes are excited.

Finally, with the development of a quantitative measure of mixedness, one can now consider mixing optimization or management, by selective enhancement or damping of specific eigenfunctions, for a wide range of applications and geometries. The technique, having been applied in this paper to experimental data, could equally well be applied to computational data.

Acknowledgments

The authors would like to thank John Ringland, Andrew Webber, and James Ferry of Brown University for their contributions to the *K-L* analysis. In addition, appreciation is given to Al Vranos and David Liscinsky of the United Technologies Research Center for providing the data used in our analysis. Finally, the authors would like to thank Harold Craig of Pratt & Whitney for his support and encouragement in this effort. R. Everson and L. Sirovich were in part supported by DARPA-URI under grant N00014-86-K0754.

References

[1]Lefebvre, A. H., *Gas Turbine Combustion,* Hemisphere, New York, 1983.

[2]Vranos, A., and Liscinsky, D. S., "Planar Imaging of Jet Mixing in Crossflow," *AIAA Journal,* Vol. 26, No. 11, 1988, pp. 1297–1298.

[3]Long, M. B., Chu, B. T., and Chang, R. K., "Instantaneous Two-Dimensional Gas Concentration Measurements by Light Scattering," *AIAA Journal,* Vol. 19, No. 9, 1981, pp. 1151–1157.

[4]Lorenz, E. N., "Prospects for Statistical Weather Forecasting," Massachusetts Inst. of Technology Final Rept., Statistical Weather Forecasting Project, Cambridge, MA, 1959.

[5]Lumley, J. L., *Atmospheric Turbulence and Radio Wave Propagation,* edited by A. M. Yaglom and V. I. Tatarski, Nauka, Moscow, 1967, pp. 166–178.

[6]Sirovich, L., "Turbulence and the Dynamics of Coherent Structures, Part I–III," *Quarterly of Applied Mathematics,* Vol. 45, No. 3, 1987, pp. 561–590.

[7]Sirovich, L., "Empirical Eigenfunctions and Low Dimensional Systems," *New Perspectives in Turbulence,* edited by L. Sirovich, Springer-Verlag, New York, 1991, pp. 139–163.

[8]Sirovich, L., and Sirovich, C., "Low Dimensional Description of Complicated Phenomena," *American Mathematical Society, Contemporary Mathematics,* Vol. 90, 1989, pp. 277–305.

[9]Breuer, K. S., and Sirovich, L., "The Use of the Karhunen-Loève Procedure for the Calculation of Linear Eigenfunction," *Journal of Computational Physics,* Vol. 96, No. 2, 1991, pp. 277–296.

[10]Sirovich, L., and Kirby, M., "Low-Dimensional Procedure for the Characterization of Human Faces," *Journal of the Optical Society of America,* Vol. 4, No. 3, 1987, pp. 519–524.

[11]Kirby, M., and Sirovich, L., "Application of the Karhunen-Loève Procedure for the Characterization of Human Faces," *IEEE Transactions on Pattern Analysis and Machine Intelligence,* Vol. 12, No. 1, 1990, pp. 103–108.

[12]Sirovich, L., Kirby, M., and Winter, M., "An Eigenfunction Approach to Large Scale Transitional Structures in Jet Flow," *Physics of Fluids A,* Vol. 2, No. 2, 1990, pp. 127–136.

[13]Hawthorne, W. R., "Secondary Circulation in Fluid Flow," *Proceedings of the Royal Society of London, Series A,* Vol. 206, 1951, pp. 347–387.

[14]Ciliberto, C., "Characterizing Space-Time Chaos in an Experiment of Thermal Convection," *Measures of Complexity and Chaos,* edited by N. B. Abraham, A. M. Albano, A. Passamante, and P. E. Rupp, Plenum Press, New York, 1989, pp. 445–456.